

# CO<sup>+</sup> first-negative band emission: A tracer for CO in the Martian upper atmosphere

Susarla Raghuram\* and Anil Bhardwaj

Physical Research Laboratory, Ahmedabad, 380009, India.

May 20, 2020

## ABSTRACT

*Context.* Recently, Imaging Ultraviolet Spectrograph (IUVS) on-board Mars Atmosphere and Volatile Evolution (MAVEN) satellite observed CO<sup>+</sup> first-negative band limb emission in the Martian upper atmosphere.

*Aims.* We aim to explore the photochemical processes in the Martian upper atmosphere, which drives this band emission.

*Methods.* A photochemical model is developed to study the excitation processes of CO<sup>+</sup> first-negative band emission ( $B^2\Sigma^+ \rightarrow X^2\Sigma^+$ ) in the upper atmosphere of Mars. The number density profiles of CO<sub>2</sub> and CO from two different models, viz., Mars Climate Database (MCD) and Mars Global Ionosphere-Thermosphere (MGIT) are used to determine the limb intensity of this band emission.

*Results.* On increasing the CO density by a factor of 4 and 8 in MCD and MGIT models, respectively, the modelled CO<sup>+</sup> first-negative band limb intensity profile is found to be consistent with IUVS/MAVEN observation. In this case, the intensity of this band emission is significantly determined by the ionization of CO by solar photons and photoelectrons, and the role of dissociative ionization of CO<sub>2</sub> is negligible.

*Conclusions.* Since CO is the major source of the CO<sup>+</sup> ( $B^2\Sigma^+$ ), we suggest that the observed CO<sup>+</sup> first-negative band emission intensity can be used to retrieve the CO density in the Martian upper atmosphere for the altitudes above 150 km.

**Key words.** Molecular processes – Planets and satellites: atmospheres – Planets and satellites: composition

## 1. Introduction

Aeronomical emissions of various excited species have been used as potential tools to study the composition of the Martian upper atmosphere (Barth et al. 1971; Strickland et al. 1972; Bertaux et al. 2005; Leblanc et al. 2006; Cox et al. 2010; Simon et al. 2009; Stiepen et al. 2015; Evans et al. 2015; Jain et al. 2015; Stevens et al. 2019; Deighan et al. 2018; Ritter et al. 2019; Gkouvelis et al. 2020; Jain et al. 2020; Qin 2020). Besides the emissions of several atomic and molecular species, the emissions from the ionic species, such as CO<sub>2</sub><sup>+</sup> (Fox-Duffendack-Barker band and ultraviolet doublet), N<sub>2</sub><sup>+</sup> (Meinel and first-negative bands), and CO<sup>+</sup> (first-negative and Comet tail bands), are also important emission features in the ultraviolet spectra. The band heads of CO<sup>+</sup> first-negative system occur nearly at the same wavelengths as that of CO Cameron band emission, which makes them challenging to observe in the Martian ultraviolet spectra. Barth et al. (1971) have reported the observation of CO<sup>+</sup> first-negative band emission ( $B^1\Sigma \rightarrow X^2\Sigma^+$ ) in the Mars during Mariner 6 and 7 experiments. However, the detection of this band emission in the Mariner 6 and 7 ultraviolet spectra is not straightforward. After subtracting the observed Martian ultraviolet spectra with the identified CO Cameron bands, the residual spectral features are ascribed to CO<sup>+</sup> first-negative band emissions. By constructing the synthetic spectra, Conway (1981) has noticed that this band emission was absent in the Mariner 9 observation. Recently, by analysing the IUVS/MAVEN observations during 6–8 April 2016, Stevens et al. (2019) reported the first-ever CO<sup>+</sup> first-negative band emission in the upper atmosphere of Mars.

The photochemical processes of the principal emissions of Martian upper atmosphere have been studied in several works by accounting for the various formation and loss mechanisms of different excited atmospheric species, (Fox & Dalgarno 1979; Mantas & Hanson 1979; Conway 1981; Shematovich et al. 2008; Simon et al. 2009; Gronoff et al. 2012b,a; Jain & Bhardwaj 2012, 2011; Gkouvelis et al. 2018; Gérard et al. 2019; Ritter et al. 2019). Photoionization of CO, photoelectron impact ionization of CO, photodissociative ionization of CO<sub>2</sub>, electron impact dissociative ionization of CO<sub>2</sub>, and resonance fluorescence of CO<sup>+</sup> are the excitation sources of CO<sup>+</sup> in  $B^2\Sigma^+$  state. By assuming different photon and electron impact cross sections of CO and CO<sub>2</sub>, Conway (1981) estimated that photodissociative ionization of CO<sub>2</sub> is the major source of this band emission in the Martian upper atmosphere. In light of the recent IUVS/MAVEN observation of CO<sup>+</sup> first-negative band emissions, we have developed a photochemical model to study the emission processes of CO<sup>+</sup> first-negative band in the Martian upper atmosphere. The main aim of the present work is to study the contribution of different excitation processes which produce CO<sup>+</sup> first-negative band emission during the IUVS/MAVEN observation. By considering different atmospheric neutral density profiles in the model, we determine the volume emission rates of CO<sup>+</sup> ( $B^2\Sigma^+$ ) and the limb intensity profiles of CO<sup>+</sup> first-negative band emission for various excitation mechanisms. We also compare our modelled limb intensity profiles with the IUVS/MAVEN observation.

## 2. Model inputs and calculations

During the IUVS/MAVEN observation period, i.e. during 6–8 April 2016, the Neutral Gas and Ion Mass Spectrometer (NGIMS) onboard MAVEN mission is also measuring the neu-

\* Corresponding author e-mail: raghuramsusarla@gmail.com

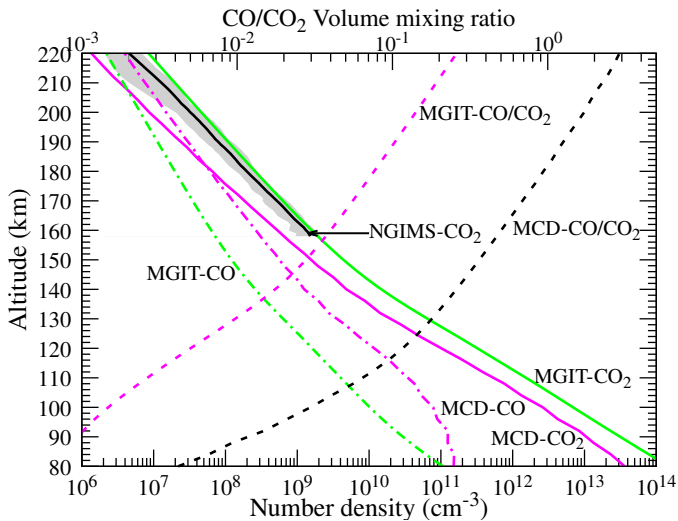


**Fig. 1.** Number density profiles of  $\text{CO}_2$  and  $\text{CO}$  from MCD and MGIT model. Solid and dash-dotted curves represent  $\text{CO}_2$  and  $\text{CO}$  density profiles, respectively. The gray shaded area represents the variation in the NGIMS/MAVEN measured  $\text{CO}_2$  density during 6–8 April 2016 for the orbits #2953–2962. The solid black curve in the shaded area represents the averaged value of  $\text{CO}_2$  from the NGIMS/MAVEN measurements. The calculated  $\text{CO}/\text{CO}_2$  volume mixing ratio profiles are plotted with dashed curves with scale on top x-axis.

tral density profiles of major species. But the NGIMS measurements of the major neutral densities are limited up to the MAVEN periapsis altitude of about 160 km. Since the peak intensity of  $\text{CO}^+$  first-negative emission is limited down to the altitude of 160 km, we used the primary neutral densities ( $\text{CO}_2$ ,  $\text{CO}$ ,  $\text{N}_2$ ,  $\text{O}_2$  and  $\text{O}$ ) from the Mars Climate Database (MCD) (version 5.3, González-Galindo et al. 2015) and Mars Global Ionosphere-Thermosphere (MGIT) (Bougher et al. 2015) models for the IUVS/MAVEN observation conditions. To compare the MCD and MGIT modelled  $\text{CO}_2$  neutral density with in-situ measurements, we analysed the NGIMS/MAVEN level 2 (L2), version 8, revision 1 data during 6–8 April 2016 for the altitudes above 160 km (<https://pds-atmospheres.nmsu.edu>). More details of the L2 data product are available in Benna & Elrod (2018). The NGIMS/MAVEN measured neutral number densities are interpolated over a uniform grid of 1 km from the periapsis altitude, i.e., 155 km to 230 km for all the orbital profiles observed during 6–8 April 2016. Figure 1 shows the  $\text{CO}_2$  and  $\text{CO}$  neutral density profiles obtained from the two models. In this figure, MGIT and MCD modelled  $\text{CO}_2$  densities are also compared with the NGIMS/MAVEN in-situ measurements.

Solar radiation flux, which is the primary energy source of Martian upper atmosphere, is taken from Solar Extreme Ultraviolet Monitor (EUVM) instrument onboard MAVEN mission measured daily-average value in the wavelength region 5–1900 Å on 7 April 2016 for orbit #2960 (Eparvier et al. 2015; Thiemann et al. 2017). A part of this solar flux spectrum is plotted in Figure 2. The photoabsorption and photoionization cross sections of the primary gases are taken from Huebner et al. (1992) (<https://phidrates.space.swri.edu>). The branching ratios for different excited states of  $\text{CO}_2^+$ ,  $\text{CO}^+$ ,  $\text{N}_2^+$ ,  $\text{O}^+$ , and  $\text{O}_2^+$  ions are taken from Avakyan et al. (1998). The photoionization and dissociative photoionization excitation cross sections of  $\text{CO}$  and  $\text{CO}_2$  producing  $\text{CO}^+(\text{B}^2\Sigma^+)$  are taken from Plummer et al. (1977) and Wu & Judge (1986), respectively. These cross sections are also plotted in Figure 2. The electron impact cross sections of  $\text{CO}_2$  and  $\text{CO}$

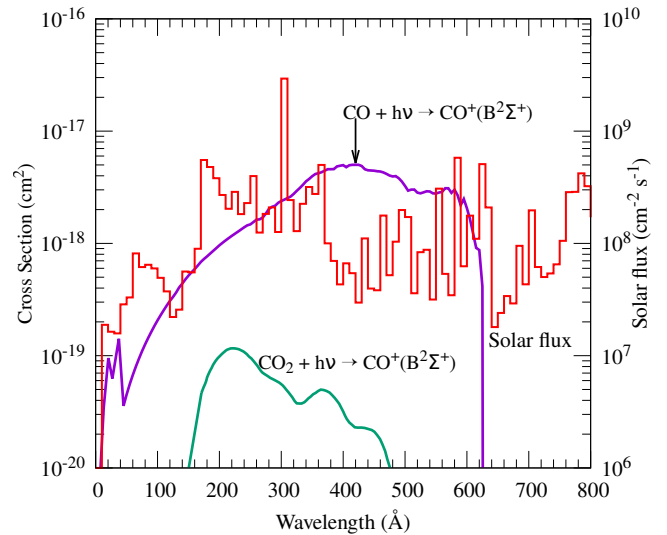


**Fig. 2.** Photoionization cross sections of  $\text{CO}_2$  and  $\text{CO}$  producing  $\text{CO}^+(\text{B}^2\Sigma^+)$ , which are taken from Wu & Judge (1986) and Plummer et al. (1977), respectively. The cross section of Wu & Judge (1986) is linearly extrapolated for the wavelength below 180 Å. The daily-averaged solar flux for the wavelengths below 800 Å, which is obtained from the measurements of Solar Extreme Ultraviolet Monitor instrument onboard MAVEN mission on 7 April 2016 for the orbit #2960 (Eparvier et al. 2015), is plotted with scale on the right y-axis.

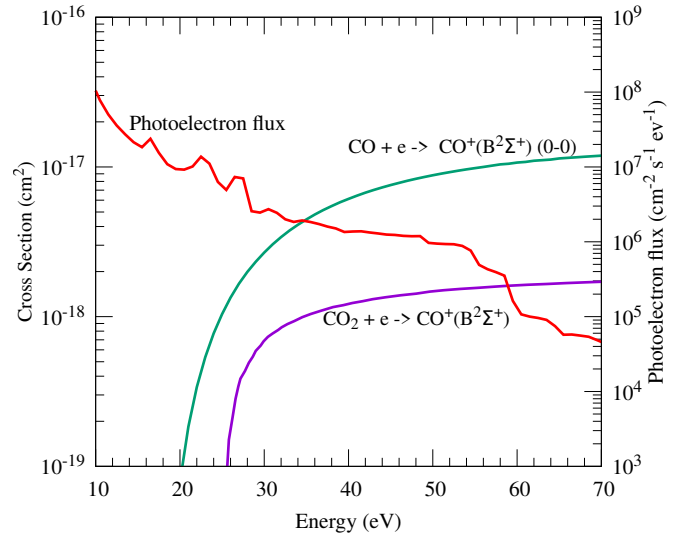


**Fig. 3.** Electron impact ionization cross sections of  $\text{CO}_2$  and  $\text{CO}$  producing  $\text{CO}^+(\text{B}^2\Sigma^+)$  which are taken from Ajello (1971) and Arqueros & Campos (1981), respectively. Modelled steady state suprathermal electron flux (red solid curve) at an altitude of 130 km using MCD neutral density profile and for SZA of  $75^\circ$  is plotted with a scale on the right y-axis.

producing  $\text{CO}^+(\text{B}^2\Sigma^+)$  are obtained from Ajello (1971) and Arqueros & Campos (1981), respectively. These cross sections are presented in Figure 3. The branching ratio for  $\text{CO}^+(\text{B}^2\Sigma^+)$  that leads to (0-0) electronic transition is taken as 0.305 (Arqueros & Campos 1982). Under photochemical equilibrium condition, the densities of major ( $\text{O}_2^+$ ,  $\text{NO}^+$ ) and minor ( $\text{CO}_2^+$ ,  $\text{CO}^+$ ,  $\text{N}_2^+$ ,  $\text{O}^+$ , and  $\text{C}^+$ ) ions are also calculated by accounting for the important production and loss mechanisms. Resonance fluorescence of  $\text{CO}^+$  producing first-negative band emission is incorporated in the model by multiplying the modelled  $\text{CO}^+$  ion density with

an emission rate (g-factor) of  $5.2 \times 10^{-5} \text{ s}^{-1}$  (Barth 1969). Scholl et al. (1998) experimentally determined the radiative lifetime of B<sup>2</sup>Σ<sup>+</sup> excited state as about 55 ns. Due to the short radiative lifetime, the collisional quenching of this excited state can be neglected. A fractional population of this excited state can decay to the ground state via A<sup>2</sup>Π<sub>u</sub> which leads to comet-tail band emission. Lawrence (1965) has determined that about 10% of CO<sup>+</sup>(B<sup>2</sup>Σ<sup>+</sup>) ions decay to A<sup>2</sup>Π<sub>u</sub> state and the rest directly decays to the ground state. Hence, we consider 90% of modelled volume emission rate leads to CO<sup>+</sup> first-negative band emission.

The modelled suprathermal electron flux in the Martian upper atmosphere at an altitude of 130 km is presented in Figure 3. Detail explanation for the calculation of steady-state suprathermal electron flux and limb emission intensities in the Martian upper atmosphere is given in our earlier works (Jain & Bhardwaj 2011, 2012). Here, we briefly describe the calculation of suprathermal electron flux spectra. Solar radiation is degraded using Beer-Lambert's law in the Martian upper atmosphere and primary photoelectron production rate spectrum Q(Z, E), at a given altitude Z as a function of energy E, is calculated using the following equation.

$$Q(Z, E) = \sum_l n_l(Z) \sum_{j,\lambda} \sigma_l^j(j, \lambda) I(Z, \lambda) \delta\left(\frac{hc}{\lambda} - E - W_{jl}\right) \quad (1)$$

$$I(Z, \lambda) = I(\infty, \lambda) \exp\left[-\sec(\chi) \sum_l \sigma_l^A(\lambda) \int_Z^\infty n(Z') dZ'\right] \quad (2)$$

Where  $\sigma_l^A(\lambda)$  and  $\sigma_l^j(j, \lambda)$  are the total photoabsorption and photoionization cross sections of  $j^{\text{th}}$  ion of the  $l^{\text{th}}$  atmospheric species at wavelength  $\lambda$ , respectively.  $I(\infty, \lambda)$  is the unattenuated solar flux at wavelength  $\lambda$  at the top of the atmosphere.  $n_l(Z)$  is the number density of  $l^{\text{th}}$  species at altitude Z.  $\chi$  is the solar zenith angle (SZA);  $\delta(hc/\lambda - E - W_{jl})$  is the delta function, in which  $hc/\lambda$  is the energy of incident photon,  $W_{jl}$  is the ionization threshold of  $j^{\text{th}}$  ionic state of the  $l^{\text{th}}$  species, and  $E$  is the energy of ejected electron. We have calculated the steady state photoelectron flux  $\phi(Z, E)$  at altitude Z and at energy E using Analytical Yield Spectrum (AYS) method using the following equation.

$$\phi(Z, E) = \int_{W_{il}}^{100} \frac{Q(Z, E) U(E, E_0)}{\sum_l n_l(Z) \sigma_{IT}(E)} dE_0 \quad (3)$$

Where,  $\sigma_{IT}(E)$  is total inelastic cross section of  $l^{\text{th}}$  species, and  $U(E, E_0)$  is the two-dimensional AYS which contains the non-spatial electron degradation information. More details of AYS method can be found in our earlier work (Singhal & Haider 1984; Bhardwaj et al. 1990, 1996; Bhardwaj 1999; Jain & Bhardwaj 2011, 2012; Bhardwaj & Jain 2013; Raghuram & Bhardwaj 2012, 2013).

We have determined the volume emission rate profiles of CO<sup>+</sup>(B<sup>2</sup>Σ<sup>+</sup>) for different electron and photon induced processes using the modelled photon and suprathermal electron fluxes and the corresponding cross sections. These modelled volume emission rate profiles are integrated along the IUVS/MAVEN tangential line of sight and converted into brightness in Rayleigh ( $1 \text{ Rayleigh} = 10^6/4\pi \text{ photons cm}^{-2} \text{ sec}^{-1} \text{ sr}^{-1}$ ) using the following equation.

$$I = 2 \times 10^{-6} \int V(r) dr \quad (4)$$

Here  $r$  is the abscissa along the horizontal line of sight, and  $V(r)$  is the volume emission rate (photons  $\text{cm}^{-3} \text{ s}^{-1}$ ) at a particular emission point  $r$  on the tangent. The factor of 2 multiplication comes due to the symmetry along the line of sight concerning the tangent point. This factor is necessary when the volume emission rate is integrated from the tangent point to infinity. The absorption of CO<sup>+</sup> first-negative band emission by other Martian species along the line of sight is negligible due to the low photoabsorption cross section.

### 3. Results and Discussion

The left and right panels of Figure 4 show the modelled volume emission rate profiles of CO<sup>+</sup>(B<sup>2</sup>Σ<sup>+</sup>) via different excitation mechanisms using the neutral density profiles from MCD and MGIT models, respectively, for the IUVS/MAVEN observational conditions at SZA of 75°. These calculations show that peak formation rate of CO<sup>+</sup>(B<sup>2</sup>Σ<sup>+</sup>) occurs at an altitude of around 140 km. On using the neutral densities from MCD model, the total volume emission rate of CO<sup>+</sup>(B<sup>2</sup>Σ<sup>+</sup>) is significantly controlled by photoionization of CO and the contribution from photon and electron impact dissociative ionization processes of CO<sub>2</sub> to the total is less than 30% (see the left panel of Fig. 4). When we use the neutral density profiles from MGIT model, about 80% of the total peak volume emission rate of CO<sup>+</sup>(B<sup>2</sup>Σ<sup>+</sup>) is controlled by dissociative ionization of CO<sub>2</sub>, whereas photoionization of CO is the important production source for the altitudes above 170 km (see the right panel of Fig. 4).

It can be noticed in Figure 1 that the CO<sub>2</sub> (CO) density profile of MGIT model is higher (lower) by about a factor of 3 (5) compared to that of MCD model. Hence, the differences in neutral densities of MCD and MGIT models lead to the photoionization of CO and photodissociative ionization of CO<sub>2</sub> to be respective major excitation sources of CO<sup>+</sup>(B<sup>2</sup>Σ<sup>+</sup>) at an altitude of around 140 km (see Fig. 4). Moreover, the difference in photon and electron impact cross sections of CO and CO<sub>2</sub> also plays an important role in determining the volume emission rate, which will be discussed later. The contribution from solar resonance fluorescence of CO<sup>+</sup> is smaller by about an order of magnitude or more to the total volume emission rate in both the modelled profiles.

Figure 5 shows a comparison between the modelled limb intensities for different excitation mechanisms, which are determined using neutral densities from MCD (left panel) and MGIT (right panel) models, and IUVS/MAVEN observation. Using the neutral density profiles from MCD model, the modelled total limb intensity profile is consistent with the lower limit of IUVS/MAVEN observation only at a few altitudes (see the left panel of Fig. 5). In this case, photon and photoelectron impact ionization processes of CO are the significant production sources to the total CO<sup>+</sup> first-negative band emission intensity. As shown in Figure 1, the CO<sub>2</sub> neutral density profile is smaller by a factor of 3 compared to the averaged value of NGIMS/MAVEN in-situ measured density for the altitudes above 160 km. To assess the role of CO<sub>2</sub> on the modelled limb intensity, we increased its neutral density profile by a factor of 3. On increasing the MCD modelled CO<sub>2</sub> density profile, the calculated total limb intensity profile is not consistent with the IUVS/MAVEN observed average intensity. But when we increase the CO neutral density profile by a factor of 3 (hereafter case-A), the modelled limb intensity profile is in agreement with IUVS/MAVEN observation. These calculations suggest that CO density plays a significant role compared to that of CO<sub>2</sub> to explain the IUVS/MAVEN observed CO<sup>+</sup> first-negative band emission profile.

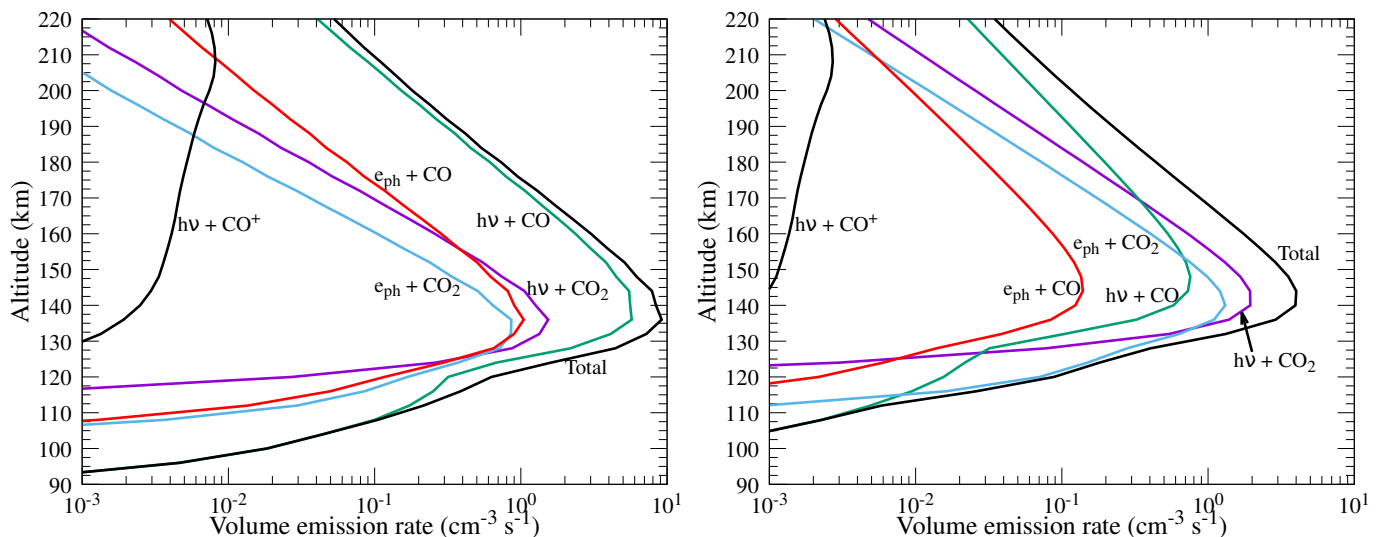


**Fig. 4.** Calculated volume emission rate profiles of  $\text{CO}^+(\text{B}^2\Sigma^+)$  in the Martian upper atmosphere via various production mechanisms using neutral density profiles from MCD (left panel) MGIT (right panel) models for SZA  $75^\circ$ .  $h\nu$  and  $e_{ph}$  represent solar photon and suprathermal electron, respectively.

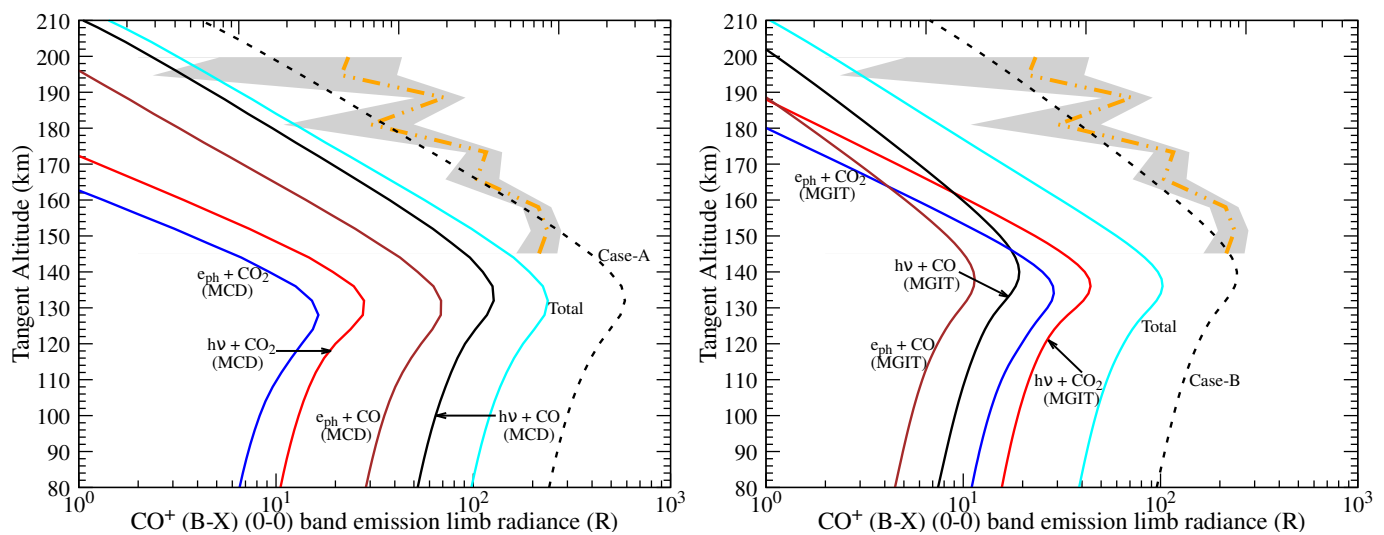


**Fig. 5.** Comparison between modelled  $\text{CO}^+$  first-negative (0-0) band emission limb intensity profiles for different excitation mechanisms, using neutral densities from MCD (left panel) and MGIT (right panel) models, and IUVS/MAVEN observation. Dash double-dotted orange curve represents the IUVS/MAVEN observed average intensity of  $\text{CO}^+$  first-negative (0-0) band emission on 7 April 2016 and the gray shaded area is its  $1-\sigma$  uncertainty (taken from Stevens et al. 2019). Here Case-A and Case-B are the modelled limb intensity profiles for the total ionization of CO (photon + photoelectron) by increasing the CO density in MCD and MGIT models by a factor of 3 and 8, respectively.  $h\nu$  and  $e_{ph}$  represent solar photon and suprathermal electron, respectively.

On using the neutral densities from MGIT model, the modelled total limb intensity is smaller by a factor of 3 or more compared to the average intensity profile of IUVS/MAVEN observation (see the right panel of Fig. 5). In this case, below 140 km altitude, photon and electron impact dissociative ionization processes of  $\text{CO}_2$  are the significant sources of  $\text{CO}^+$  first-negative band emission. Above 160 km radial distance, the contribution from CO is important to the total emission intensity. Since the  $\text{CO}_2$  neutral density of MGIT model is consistent with NGIMS/MAVEN in-situ measurements (see Fig. 1), we assess the impact of CO density on the modelled limb emission intensity. By increasing the MGIT CO neutral density profile by a factor of 8 (hereafter Case-B), the modelled limb intensity is found to be in agreement with the IUVS/MAVEN observation. This calculation also suggests that a higher amount of CO is

required to explain the IUVS/MAVEN observed emission profile. By considering the variability in  $\text{CO}_2$  density as measured by NGIMS/MAVEN (a factor of 2–5, as shown in Fig. 1), no agreement was found between the modelled limb intensity profile for the dissociative ionization of  $\text{CO}_2$  and the IUVS/MAVEN observation, which also suggests that  $\text{CO}_2$  is not a suitable candidate to explain the observed  $\text{CO}^+$  first-negative band emission. For the above all cases, the contribution from solar resonance is very small ( $<1$  R) hence it is not shown in Figure 5.

We also explored the role of thermosphere temperature, which determines the scale heights of  $\text{CO}_2$  and CO densities, during the IUVS/MAVEN observation period. By analysing the NGIMS and IUVS measurements, Bougher et al. (2017) have studied the structure and variability of Martian dayside thermosphere during MAVEN observation period, i.e. October 2014 to

May 2016. This analysis shows that the mean temperature of the Martian upper atmosphere, during the period 22 March 2016 to 10 April 2016 for the orbits #2873–2974, was around 195 K with a variability of 155–225 K (see Figure 2 of [Bougher et al. 2017](#)). IUVS/MAVEN observed the CO<sup>+</sup> first-negative band emission on 7 April 2016 for the orbits #2953–2962 ([Stevens et al. 2019](#)), and during this period the derived mean temperature of the thermosphere from the MAVEN observations was below 225 K. Moreover, as shown in Figure 1, the variation in NGIMS/MAVEN measured CO<sub>2</sub> neutral density is also small (by a factor ~2 to 5). Thus, during the IUVS/MAVEN observation period, the derived lower thermosphere temperature (<225 K), lack of substantial variability in the in-situ measured CO<sub>2</sub> neutral density, and the lower contribution of dissociative excitation of CO<sub>2</sub> (see Fig. 5) also confirm that the dissociative ionization of CO<sub>2</sub> can not be a significant excitation source to explain the observed limb intensity profile.

The smaller value of photon and electron impact dissociative excitation cross sections of CO<sub>2</sub> compared to that of CO is also another main reason for CO<sub>2</sub> not being a potential source of CO<sup>+</sup> first-negative band emission (see Figs. 2 and 3). Using the experimentally determined photoionization cross sections and on-board measured solar flux, we calculated the unattenuated photoionization excitation frequencies of CO<sub>2</sub> and CO producing CO<sup>+</sup>(B<sup>2</sup>Σ<sup>+</sup>) as  $5.5 \times 10^{-10}$  and  $1 \times 10^{-8}$  s<sup>-1</sup>, respectively. Due to the large flux, the solar radiation at the wavelength He II 303 Å significantly determines these modelled photoionization excitation frequencies (see Fig. 2). Our calculated photoionization excitation frequencies show that the formation of CO<sup>+</sup>(B<sup>2</sup>Σ<sup>+</sup>) via CO channel is 20 times more efficient compared to that of CO<sub>2</sub> per molecule. Hence, though the number density is small, CO significantly controls the CO<sup>+</sup>(B<sup>2</sup>Σ<sup>+</sup>) formation and subsequently CO<sup>+</sup> first-negative band emission intensity in the Martian upper atmosphere for the altitudes above 150 km. Moreover, due to the difference in scale heights, the CO<sub>2</sub> neutral density decreases with altitude much faster than that of CO which leads to a progressive decrease in the contribution from CO<sub>2</sub> to the total CO<sup>+</sup> first-negative band emission above the homopause (see Fig. 5).

Besides the role of number densities, we also studied the impact of uncertainties associated with the measurement of photon and electron impact ionization cross sections of CO and CO<sub>2</sub> and the solar flux on the modelled limb intensity profiles. As mentioned earlier, the photon cross sections of CO and CO<sub>2</sub> producing CO<sup>+</sup>(B<sup>2</sup>Σ<sup>+</sup>) are taken from [Plummer et al. \(1977\)](#) and [Wu & Judge \(1986\)](#), respectively. [Wu & Judge \(1986\)](#) have not mentioned the uncertainty in their measured photoionization cross section of CO<sub>2</sub>. Even on increasing this cross section by a factor of 2 no agreement was found between modelled limb intensity profile and the IUVS/MAVEN observation. For CO, [Plummer et al. \(1977\)](#) have determined the photoionization cross section of CO<sup>+</sup>(B<sup>2</sup>Σ<sup>+</sup>) using their experimentally measured branching ratios and total absorption cross section, which is also consistent with the earlier experimental determination by [Samson et al. \(1976\)](#) and [van der Wiel & Brion \(1972\)](#). [Samson et al. \(1976\)](#) has evaluated that the statistical error in the measured branching ratios is less than 10%. Thus, the effect of uncertainty in the measured photoionization cross section of CO has a small impact on the modelled limb emission intensities.

The uncertainties associated with the measured electron impact cross sections of CO<sub>2</sub> and CO by [Ajello \(1971\)](#) and [Arequeros & Campos \(1981\)](#), respectively, are about 25%. However, it should be noted that the photoionization excitation rates of CO<sub>2</sub> and CO producing CO<sup>+</sup>(B<sup>2</sup>Σ<sup>+</sup>) are higher by a factor

2 or more compared to those of electron impact ionization (see Fig. 4). Thus, the role of uncertainties in the measured electron impact cross sections on the modelled limb intensity profiles can be neglected. Regarding the uncertainty in the solar flux, [Thiemann et al. \(2017\)](#) have studied that about a maximum of 30% uncertainty is possible in the daily measured solar flux for the wavelengths less than 700 Å in the Flare Irradiance Spectral Model on Mars (FISM-M). Hence, for given CO and CO<sub>2</sub> density profiles, we estimate that the uncertainties associated with the cross sections and the solar flux can lead to about a maximum of 40–50% uncertainty in the modelled limb intensity.

On 2016 April 07, IUVS measured CO<sup>+</sup> first-negative band emission intensity with a standard deviation of one  $\sigma$  ([Stevens et al. 2019](#)). But it can be noticed in Figure 5 that for the altitudes above 170 km, the observed CO<sup>+</sup> first-negative band emission intensity vary significantly. Considering this variation into account, we varied the CO densities in MCD and MGIT models to reconcile the IUVS/MAVEN observation. We find a factor of 6–10 and 3–5 increment is required for CO density profiles of MGIT and MCD models, respectively, to explain the observed emission intensity profile. This calculation suggests that during IUVS observation period CO density may be varying significantly along the IUVS/MAVEN line of sight. However, there are no NGIMS/MAVEN in-situ measured CO density profiles available to study the variation in IUVS/MAVEN observed CO<sup>+</sup> first-negative band intensity.

The CO is an important minor species in the Martian upper atmosphere, which plays a significant role in maintaining the stability of CO<sub>2</sub> via a photochemical cycle. The direct recombination of CO and O, which are dissociative products of CO<sub>2</sub>, is forbidden. Hence, this reaction can not be an effective mechanism to recycle CO<sub>2</sub> in the Martian upper atmosphere. By invoking heterogeneous chemistry, several modelling works were carried out to study the stability of CO<sub>2</sub> in the Martian atmosphere ([McElroy & Hunten 1970](#); [McElroy et al. 1976](#); [Nier & McElroy 1977](#); [Krasnopolsky 1993](#); [Nair et al. 1994](#); [Atreya & Gu 1994, 1995](#)). Since CO primarily originates from the photodissociation of CO<sub>2</sub>, the variation in CO<sub>2</sub> density will have a direct impact on the CO abundance. Besides the variation in CO<sub>2</sub> neutral density, the chemical loss reaction between OH and CO, which consequently recycle the CO<sub>2</sub>, also determines the concentration of CO in the Martian upper atmosphere ([Nair et al. 1994](#); [González-Galindo et al. 2005](#)). As shown earlier, when we use a larger amount of CO than MCD and MGIT modelled values, the modelled limb intensity profile for case-A and case-B are in agreement with the IUVS/MAVEN observation (see Fig. 5). Since no strong variability in the NGIMS/MAVEN measured CO<sub>2</sub> number density is seen (with a variation of factor 2 from the mean value, see Fig. 1) and also the derived thermosphere temperature is low (~200 K, see [Bougher et al. 2015](#)), the larger amount of CO density in the Martian upper atmosphere is only possible if its chemical loss rate is significantly low during the IUVS observation period. By analysing the Compact Reconnaissance Imaging Spectrometer for Mars (CRISM) instrument onboard Mars Reconnaissance Orbiter (MRO) data, [Smith et al. \(2018\)](#) have also shown that CO density can undergo a strong seasonal variation. Hence, the collisional chemistry of CO strongly determines its neutral density in the Martian upper atmosphere and consequently the observed CO<sup>+</sup> first-negative emission intensity.

As shown in Figure 1, the CO<sub>2</sub> density profiles of MCD and MGIT models are closer to the NGIMS/MAVEN in situ measurements. However, it should be noticed that the CO<sub>2</sub> density of MCD model is smaller than that of MGIT model by a factor 3 to 5. But in contrast, the CO density of MCD model is higher com-

pared to that of MGIT model by a factor 2 to 10. The differences between CO and CO<sub>2</sub> densities of these models lead to an order of magnitude higher CO/CO<sub>2</sub> volume mixing ratio in the MCD model when compared to that in the MGIT model (see dashed curves in Fig. 1). This significant change in the CO/CO<sub>2</sub> volume mixing ratios may be due to the photochemistry of CO incorporated in these general circulation models. Though the major photochemical production and loss reactions of CO are incorporated in these models, the CO density profiles in both models are not sufficient to explain the IUVS/MAVEN observation. This suggests that probably the CO density profiles are underestimated during the IUVS/MAVEN observation period. Hence, based on our model calculations, we suggest that the role of CO is more important than that of CO<sub>2</sub> and the observed limb intensity profile of this band emission can be used as a good tracer to study the CO volume mixing ratio and also its seasonal variation for the altitudes above 150 km. The retrieval of CO density profiles based on the CO<sup>+</sup> first-negative band also helps to understand the production and loss of CO, which is primarily linked with CO<sub>2</sub> density and also collisional chemistry, in the Martian upper atmosphere. However, it should be noted the thermospheric temperature can play an important role in determining the CO<sub>2</sub> density at the altitudes above 150 km. Using CO<sub>2</sub><sup>+</sup> ultraviolet doublet emission at 289 nm, Jain et al. (2020) recently measured first-ever thermospheric temperature at an altitude of 170 km during the planetary encircling dust event of 2018. They observed that the mean temperature of thermosphere can be increased as high as 20 K at higher latitudes during the global dust event. Thus for high thermosphere temperature (about 300 K), the contribution of CO<sub>2</sub>, via photon and electron impact dissociative ionization, can also be significant to the total CO<sup>+</sup> first-negative band emission. Hence, modelling of this band emission by incorporating the primary production processes is essential to derive the CO density based on the observed emission intensity profiles.

#### 4. Summary and Conclusions

IUVS onboard MAVEN mission recently observed first-ever CO<sup>+</sup> first-negative band emission in the Martian upper atmosphere (Stevens et al. 2019). We have studied the photochemistry of this band emission by incorporating various CO<sup>+</sup>(B<sup>2</sup>Σ<sup>+</sup>) formation processes and the neutral densities of the upper atmosphere from MCD and MGIT models. By comparing the modelled limb intensity profiles with the IUVS/MAVEN measurements, we found that CO<sub>2</sub> is not a suitable candidate to explain the observed intensity profile of CO<sup>+</sup> first-negative band emission. By increasing the input CO density (by a factor of 3 and 8 in MCD and MGIT models, respectively), the modelled CO<sup>+</sup> first-negative band intensity profile is in agreement with IUVS/MAVEN observation, which suggests that a large amount of CO was present during the observation period. In this case, the observed emission intensity is significantly governed by the ionization of CO, by both photons and electrons. Since CO significantly contributes to this emission, we suggest that the observed band intensity can be used to retrieve CO abundance in the Martian upper atmosphere for the altitudes above 150 km. The derivation of CO density based on the observed CO<sup>+</sup> first-negative emission intensity profile also helps to constrain its volume mixing ratio in the general circulation models as well as to study the stability of CO<sub>2</sub> in the Martian upper atmosphere. More observations of this band emission along with modelling are essential to constrain the CO volume mixing ratio and its variation during different seasonal conditions in the Martian upper atmosphere.

*Acknowledgements.* The neutral and ion number densities used in the present study have been taken from MAVEN/NGIMS data which is accessible through the web link <https://pds-atmospheres.nmsu.edu>. We would like to thank Prof. Stephen Bougher for providing the neutral density profiles from MGIT model. SR is supported by Department of Science and Technology (DST) with Innovation in Science Pursuit for Inspired Research (INSPIRE) faculty award [grant:dst/inspire/04/2016/002687], and he would like to thank Physical Research Laboratory for facilitating conducive research environment. The authors would like to thank the reviewer for the valuable comments and suggestions that improved the manuscript.

#### References

- Ajello, J. M. 1971, *J. Chem. Phys.*, 55, 3169  
 Arqueros, F. & Campos, J. 1981, *Journal of Physics B Atomic Molecular Physics*, 14, 2159  
 Arqueros, F. & Campos, J. 1982, *Physica*, 112, 131  
 Atreya, S. K. & Gu, Z. G. 1994, *J. Geophys. Res.*, 99, 13133  
 Atreya, S. K. & Gu, Z. G. 1995, *Advances in Space Research*, 16, 57  
 Avakyan, S. V., Il'in, R. N., Lavrov, V. M., & Ogurtsov, G. N., eds. 1998, *Collision Processes and Excitation of UV Emission from Planetary Atmospheric Gases: A Handbook of Cross Sections* (Gordon and Breach Science Publishers)  
 Barth, C. A. 1969, *Appl. Opt.*, 8, 1295  
 Barth, C. A., Hord, C. W., Pearce, J. B., et al. 1971, *J. Geophys. Res.*, 76, 2213  
 Benna, M. & Elrod, M. 2018, *NGIMS PDS Software Interface Specification, Revision 1.9*  
 Bertaux, J.-L., Leblanc, F., Witasse, O., et al. 2005, *Nature*, 435, 790  
 Bhardwaj, A. 1999, *J. Geophys. Res.*, 104, 1929  
 Bhardwaj, A., Haider, S. A., & Singhal, R. P. 1990, *Icarus*, 85, 216  
 Bhardwaj, A., Haider, S. A., & Singhal, R. P. 1996, *Icarus*, 120, 412  
 Bhardwaj, A. & Jain, S. K. 2013, *Journal of Geophysical Research (Space Physics)*, 118, 3660  
 Bougher, S. W., Pawlowski, D., Bell, J. M., et al. 2015, *Journal of Geophysical Research (Planets)*, 120, 311  
 Bougher, S. W., Roeten, K. J., Olsen, K., et al. 2017, *Journal of Geophysical Research (Space Physics)*, 122, 1296  
 Conway, R. R. 1981, *J. Geophys. Res.*, 86, 4767  
 Cox, C., Gérard, J. C., Hubert, B., Bertaux, J. L., & Bougher, S. W. 2010, *J. Geophys. Res.*, 115, E04010  
 Deighan, J., Jain, S. K., Chaffin, M. S., et al. 2018, *Nature Astronomy*, 2, 802  
 Eparvier, F. G., Chamberlin, P. C., Woods, T. N., & Thiemann, E. M. B. 2015, *Space Sci. Rev.*, 195, 293  
 Evans, J. S., Stevens, M. H., Lumpe, J. D., et al. 2015, *Geophys. Res. Lett.*, 42, 9040  
 Fox, J. L. & Dalgarno, A. 1979, *J. Geophys. Res.*, 84, 7315  
 Gérard, J.-C., Gkouvelis, L., Ritter, B., et al. 2019, *Journal of Geophysical Research: Space Physics*, 124, 5816  
 Gkouvelis, L., Gérard, J. C., Ritter, B., et al. 2018, *Journal of Geophysical Research (Planets)*, 123, 3119  
 Gkouvelis, L., Gérard, J. C., Ritter, B., et al. 2020, *Icarus*, 341, 113666  
 González-Galindo, F., López-Valverde, M. A., Angelats i Coll, M., & Forget, F. 2005, *Journal of Geophysical Research (Planets)*, 110, E09008  
 González-Galindo, F., López-Valverde, M. A., Forget, F., et al. 2015, *Journal of Geophysical Research (Planets)*, 120, 2020  
 Gronoff, G., Wedlund, C. S., Mertens, C. J., et al. 2012a, *Journal of Geophysical Research (Space Physics)*, 117, A05309  
 Gronoff, G., Wedlund, C. S., Mertens, C. J., & Lillis, R. J. 2012b, *Journal of Geophysical Research (Space Physics)*, 117, A04306  
 Huebner, W. F., Keedy, J. J., & Lyon, S. P. 1992, *Astrophys. Space Sci.*, 195, 1  
 Jain, S. K. & Bhardwaj, A. 2011, *Journal of Geophysical Research (Planets)*, 116, E07005  
 Jain, S. K. & Bhardwaj, A. 2012, *Planetary and Space Science*, 64, 110  
 Jain, S. K., Bougher, S. W., Deighan, J., et al. 2020, *Geophys. Res. Lett.*, 47, e85302  
 Jain, S. K., Stewart, A. I. F., Schneider, N. M., et al. 2015, *Geophys. Res. Lett.*, 42, 9023  
 Krasnopolsky, V. A. 1993, *Icarus*, 101, 33  
 Lawrence, G. 1965, *J. Quant. Spectr. Rad. Transf.*, 5, 359  
 Leblanc, F., Chaufray, J. Y., Lilensten, J., Witasse, O., & Bertaux, J. L. 2006, *Journal of Geophysical Research (Planets)*, 111, E09S11  
 Mantas, G. P. & Hanson, W. B. 1979, *J. Geophys. Res.*, 84, 369  
 McElroy, M. B. & Hunten, D. M. 1970, *J. Geophys. Res.*, 75, 1188  
 McElroy, M. B., Kong, T. Y., Yung, Y. L., & Nier, A. O. 1976, *Science*, 194, 1295  
 Nair, H., Allen, M., Anbar, A. D., Yung, Y. L., & Clancy, R. T. 1994, *Icarus*, 111, 124

- Nier, A. O. & McElroy, M. B. 1977, *J. Geophys. Res.*, 82, 4341
- Plummer, E. W., Gustafsson, T., Gudat, W., & Eastman, D. E. 1977, *Phys. Rev. A*, 15, 2339
- Qin, J. 2020, *AJ*, 159, 206
- Raghuram, S. & Bhardwaj, A. 2012, *Planet. Space Sci.*, 63, 139
- Raghuram, S. & Bhardwaj, A. 2013, *Icarus*, 223, 91
- Ritter, B., Gérard, J. C., Gkouvelis, L., et al. 2019, *Journal of Geophysical Research (Space Physics)*, 124, 4809
- Samson, J. A. R., Bougher, J. L., & Gardner. 1976, *Journal of Electron Spectroscopy and Related Phenomena*, 8, 35
- Scholl, T. J., Rosner, S. D., & Holt, R. A. 1998, *Canadian Journal of Physics*, 76, 39
- Shematovich, V. I., Bisikalo, D. V., Gérard, J. C., et al. 2008, *Journal of Geophysical Research (Planets)*, 113, E02011
- Simon, C., Witasse, O., Leblanc, F., Gronoff, G., & Bertaux, J. L. 2009, *Planet. Space Sci.*, 57, 1008
- Singhal, R. P. & Haider, S. A. 1984, *J. Geophys. Res.*, 89, 6847
- Smith, M. D., Daerden, F., Neary, L., & Khayat, A. 2018, *Icarus*, 301, 117
- Stevens, M. H., Siskind, D. E., Evans, J. S., et al. 2019, *Journal of Geophysical Research (Planets)*, 124, 1226
- Stiepen, A., Gérard, J. C., Bougher, S., et al. 2015, *Icarus*, 245, 295
- Strickland, D. J., Thomas, G. E., & Sparks, P. R. 1972, *J. Geophys. Res.*, 77, 4052
- Thiemann, E. M. B., Chamberlin, P. C., Eparvier, F. G., et al. 2017, *Journal of Geophysical Research (Space Physics)*, 122, 2748
- van der Wiel, M. J. & Brion, C. 1972, *Journal of Electron Spectroscopy and Related Phenomena*, 1, 309
- Wu, C. Y. R. & Judge, D. L. 1986, *J. Chem. Phys.*, 84, 4720